

from the agri-expert system is near to true value with greater accuracy which can be enhanced the decision making ability of end users for the betterment of farming community.

The findings of the present study confirm that more respondents belonged to 'innovators' category with special reference to the use of KAU expert system when compared to Roger's standard. Innovation proneness was positively and significantly related with the extent of adoption of the expert system among all three categories of respondents. Even though a fair percentage of respondents belonged to the 'innovators/early adopters/early majority' category, there was a gap between laggards and innovators. This gap should be reduced by imparting proper training for augmenting the usage of agri-expert systems for effective decision-making with precise, correct and timely information.

1. Waterman, D. A., *A Guide to Expert Systems*, Pearson Education, Delhi, 2004, p. 419.
2. Plant, R. E. and Stone, N. D., *Knowledge-Based Systems in Agriculture*, McGraw-Hill, NY, USA, 1991, p. 364.
3. Chetsumon, S., Attitudes of extension agents towards expert systems as decision support tools in Thailand. Ph D thesis, Lincoln University, Thailand, 2005.
4. Rogers, E., Categorizing the adopters of agricultural practices. *Rural Sociol.*, 1958, **23**, 345–354.
5. Ortt, J. and Schoormans, J. P. L., The pattern of development and diffusion of breakthrough communication technologies. *Eur. J. Innov. Manage.*, 2004, **7**(4), 292.

**ACKNOWLEDGEMENTS.** This study is a part of the PG research programme in the College of Agriculture, Vellayani, Thiruvananthapuram, Kerala, India. We thank KAU, Thrissur, Kerala for providing financial support to conduct this study and all the respondents who helped complete the study within the stipulated time-frame.

Received 25 October 2016; revised accepted 23 January 2017

doi: 10.18520/cs/v112/i11/2284-2288

## Comparative analysis of spectral characteristics of EO-1 ALI and Landsat 8 OLI imagery

Xuehong Zhang<sup>1,2,\*</sup> and Lixin Shi<sup>2</sup>

<sup>1</sup>School of Geography and Remote Sensing, Nanjing University of Information Science and Technology, Nanjing 210044, China

<sup>2</sup>Hebei Provincial Key Lab for Meteorology and Eco-environment, Meteorological Institute of Hebei Province, Shijiazhuang 050021, China

**Landsat 8 (L8) is the only normally operating Landsat satellite at present, and the Earth Observing One (EO-1) Advanced Land Imager (ALI) was the prototype for operational land imager (OLI) on-board the L8 satellite. To comprehend well the differences in spectral characteristics between the two sensors, six nearly simultaneous image pairs were selected, which included five land-cover categories: water, bare soil, vegetation, manmade and rock. Moreover, comparisons of spectral characteristics were made through orbital parameters, imaging parameters, spectral response characteristics and spectral characteristics. Finally, the mutual quantitative relations were built up among these image pairs. The results demonstrate that Landsat 8 OLI and EO-1 ALI have similar orbital parameters. With regard to the imaging and spectral response characteristics, the top-of-atmosphere (TOA) reflectance and normalized difference vegetation index (NDVI) of EO-1 ALI are slightly different from those of L8 OLI, but there is a high correlation between EO-1 ALI and L8 OLI of TOA reflectance and NDVI, with the coefficients of determination ranging from 0.962 to 0.994. Therefore, the TOA reflectance and NDVI images from the two sensors are complementary.**

**Keywords:** Top-of-atmosphere reflectance, spectral characteristics, image pairs, vegetation index.

To probe and quantify long-term changes in the earth's environment using satellites, one usually relies on multi-sensors and multi-date datasets. However, the quality of remote-sensing images varies as a result of atmospheric attenuation, sun-looking geometry parameters, orbital and imaging parameters, etc.<sup>1</sup>. Consequently, to monitor changes over time, it is crucial to comprehend the discrepancies between different remote sensors.

Landsat-8 (L8) launched on 11 February 2013, is the only normally operating Landsat satellite at present. It carries two sensors, Operational Land Imager (OLI) and Thermal Infrared Sensor (TIRS). Earth Observing One (EO-1), launched on 21 November 2000, has three sensors on-board, including the Atmospheric Corrector

\*For correspondence. (e-mail: zxhbnu@126.com)

**Table 1.** Key specifications of EO-1 and L8

Platform	EO-1	L8
Sensor	ALI	OLI
Launch date	21 November 2000	11 February 2013
Number of bands	10	9
GSD (ground sampling distance; m)	10, 30	15, 30
Swath (km)	37	185
Pixel quantization (bits)	12	12
Orbit type	Sun-synchronous	Sun-synchronous
Equatorial crossing time	10 : 01 a.m. $\pm$ 15 min	10 : 00 a.m. $\pm$ 15 min
Altitude (km)	705	705
Repeat cycle (days)	16	16

**Table 2.** Spectral coverage, GSD, mean solar exoatmospheric irradiance (ESUN <sub>$\lambda$</sub> ) and calibration coefficients of EO-1 ALI sensor

Band	Spectral range ( $\mu\text{m}$ )	GSD (m)	ESUN <sub><math>\lambda</math></sub> ( $\text{Wm}^{-2} \mu\text{m}^{-1}$ )	Gain ( $\text{W m}^{-2} \text{sr}^{-1} \mu\text{m}^{-1}$ )/(DN)	Offset ( $\text{Wm}^{-2} \text{sr}^{-1} \mu\text{m}^{-1}$ )
EO-1 ALI					
1P	0.433–0.453	30	1857	0.045	–3.4
1	0.450–0.515	30	1996	0.043	–4.4
2	0.525–0.605	30	1807	0.028	–1.9
3	0.630–0.690	30	1536	0.018	–1.3
4	0.775–0.805	30	1145	0.011	–0.85
4P	0.845–0.890	30	955.8	0.0091	–0.65
5P	1.200–1.300	30	452.3	0.0083	–1.3
5	1.550–1.750	30	235.1	0.0028	–0.6
7	2.080–2.350	30	82.38	0.00091	–0.21
Pan	0.480–0.690	10	1724	0.024	–2.2

\*From ref. 16.

(AC), Hyperion and Advanced Land Imager (ALI)<sup>2</sup>. EO-1 has been continuously obtaining data since then<sup>2</sup>. The ALI data were frequently employed to compare them with data of other satellites, such as Landsat 7 ETM+ (refs 3–7), MODIS<sup>4,7</sup>, LISS-III (ref. 1) and Landsat 5 Thematic Mapper (TM)<sup>8,9</sup>.

Top-of-atmosphere (TOA) reflectance is used to estimate the vegetation index (VI)<sup>10–12</sup>. VI has been extensively used to describe the vegetation cover condition and the growing state of vegetation qualitatively and quantitatively<sup>13</sup>. VI derived from TOA reflectance is closely connected with the vegetation biomass and leaf area index (LAI) of canopies<sup>14</sup>. These indices are usually applied in many ecological models using remotely sensed information as the driving variable<sup>11,14</sup>. Normalized difference vegetation index (NDVI) is a universally utilized index among VIs. It is recommended for the comparison of cross-sensor VIs<sup>15</sup>.

Combining the analysis of orbital and imaging parameters, spectral response characteristics, NDVI and TOA reflectance, this communication aims to compare spectral characteristics of L8 OLI imagery with those of EO-1 ALI imagery, and to evaluate differences in spectral characteristics such as TOA and NDVI between OLI and ALI.

Table 1 displays the orbital parameters of L8 and EO-1, such as orbit type, equatorial crossing time, altitude, repeat cycle. Tables 1–3 compare the imaging parameters of ALI and OLI. The swath width of OLI is 185 km and it is for ALI 37 km. The data quantization for ALI and OLI is 12 bits respectively. EO-1 and L8 have the same spatial resolution for their multispectral bands, i.e. 30 m. There are seven similar bands between ALI and OLI (viz. OLI 1, OLI 2, OLI 3, OLI 4, OLI 5, OLI 6 and OLI 7) (Table 2 and Figure 1).

Figure 1 displays the relative spectral response (RSR) functions of L8 OLI and EO-1 ALI, and the spectral reflectance curves of some typical targets such as vegetation, soil and water. ALI has two narrow near-infrared (NIR) bands, namely ALI 4 and ALI 4P (ref. 1). However, L8 OLI is designed with only one NIR band, and the spectral range of OLI5 overlaps ALI 4P. Bandwidth of ALI is wider compared to that of L8 in the corresponding bands, except OLI 1 and OLI 2.

To compare the spectral characteristics of the two sensors, the near-simultaneous images acquired by the remote sensors should be chosen. Here, six synchronous image pairs were chosen from China for EO-1 ALI and L8 OLI (Table 4). Each image pair has a similar solar zenith angle. The difference in imaging time is within

**Table 3.** Spectral coverage, GSD, mean solar exoatmospheric irradiance ( $ESUN_{\lambda}$ ) and calibration coefficients of L8 OLI sensor

Band	Spectral range ( $\mu\text{m}$ )	GSD (m)	*Multiplicative rescaling factor	*Additive rescaling factor
L8 OLI				
1	0.433–0.453	30	0.00002	-0.1
2	0.450–0.515	30	0.00002	-0.1
3	0.525–0.600	30	0.00002	-0.1
4	0.630–0.680	30	0.00002	-0.1
5	0.845–0.885	30	0.00002	-0.1
6	1.560–1.660	30	0.00002	-0.1
7	2.100–2.300	30	0.00002	-0.1
8	0.500–0.680	15	0.00002	-0.1
9	1.360–1.390	30	0.00002	-0.1

\*TOA reflectance rescaling coefficients.

**Table 4.** Common OLI and ALI image pairs used here

Location (in China)	Date	Scene centre		Sensor	Path/row	Solar elevation ( $^{\circ}$ )
		scan time (GMT)				
Dunhuang City, Qinghai Province	2013/05/14	03:54	ALI	137/32	59.03	
		04:21	OLI			
Nantou County, Taiwan Province	2013/07/05	01:51	ALI	117/44	60.47	
		02:23	OLI			
Wuyuan County, Inner Mongolia Autonomous Region	2013/09/11	03:00	ALI	129/31	46.71	
		03:32	OLI			
Qitai County, Xinjiang Uygur Autonomous Region	2013/12/04	04:11	ALI	141/29	21.79	
		04:45	OLI			
Zhaoqing City, Guangdong Province	2013/12/06	02:15	ALI	123/44	35.18	
		02:59	OLI			
Dunhuang City, Qinghai Province	2014/03/14	03:37	ALI	137/32	37.46	
		04:20	OLI			

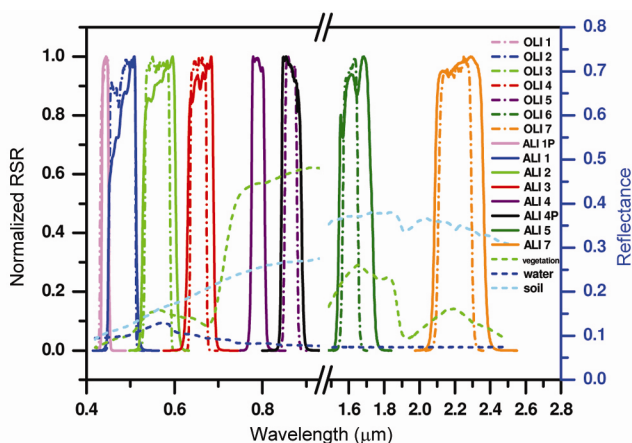


**Figure 1.** Relative spectral response (RSR) of EO-1 ALI and L8 OLI in the corresponding bands and spectral reflectance curves of some typical targets (e.g. vegetation, soil and water).

45 min between EO-1 ALI and L8 OLI. One can assume that the atmosphere condition is similar for each image pair<sup>1</sup>. Land-cover types of these test sites include water, vegetation, rock, man-made and bare soil.

Topographic effect usually results in different radiance for the images acquired by the remote sensors. The dif-

ferences are related to the geometric position of sun-satellite-target. The very small regions of interest (ROIs) for each land-cover category from these image pairs were chosen in order to weaken the topographic effect. Moreover, it is helpful to compare the spectral characteristics for each ROI by statistical analysis on spectral reflectance (e.g. mean and standard deviation). This can also effectively reduce the geometric correction errors. Finally, 71 ROIs were chosen from the 6 image pairs with pixels more than 50 for each ROI, which included 13 water ROIs, 18 vegetation ROIs, 25 bare soil ROIs, 5 man-made ROIs and 10 rock ROIs.

There is usually a linear relationship between the response of remote sensor detectors and incoming radiance. Depending on the sensor, this response is quantized into different digital numbers (DNs) representing brightness values. The DN<sub>s</sub> can be converted to apparent radiance by calibration coefficients<sup>1</sup>. The TOA reflectance is then computed as

$$\rho_{TOA} = \frac{\pi L_{\lambda} d^2}{ESUN_{\lambda} \cos \theta_s}, \tag{1}$$

where  $\rho_{TOA}$  is the TOA reflectance,  $ESUN_{\lambda}$  the mean solar exoatmospheric irradiance,  $L_{\lambda}$  the apparent radiance,  $d$

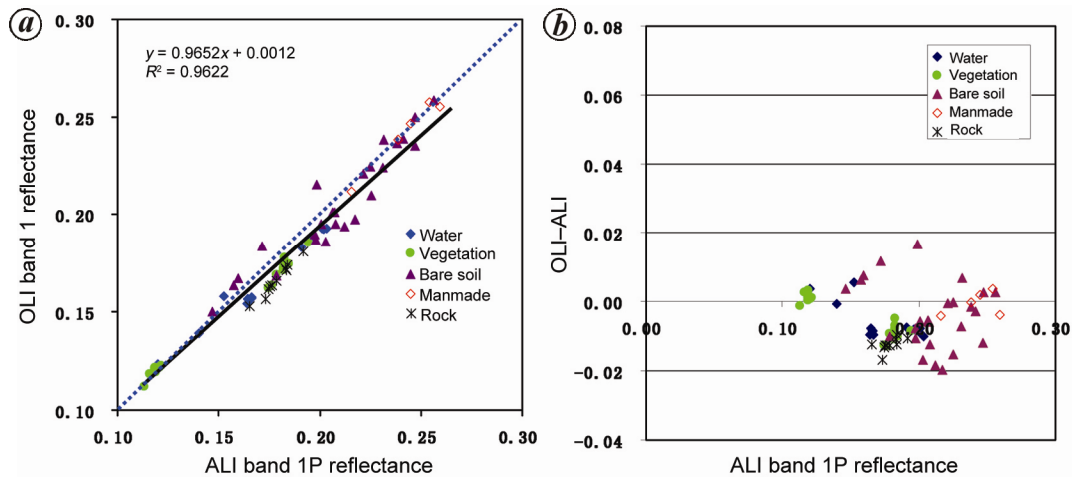


**Figure 2.** Scatter plots of (a) mean TOA reflectance of all ROIs for OLI and ALI images in the blue band (OLI 1 versus ALI 1P) and (b) absolute difference in TOA reflectance for OLI in comparison to ALI as a function of TOA reflectance from ALI.

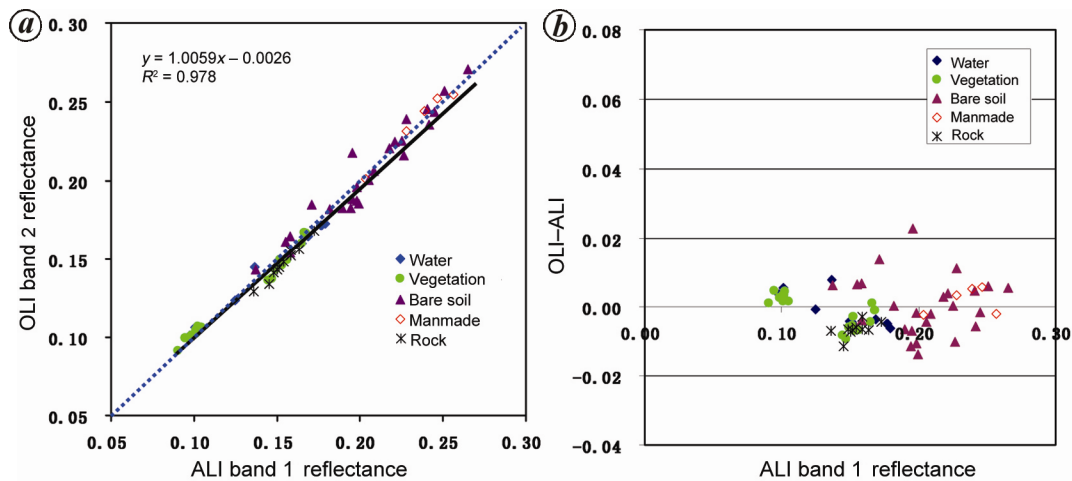


**Figure 3.** Scatter plots of (a) mean TOA reflectance of all ROIs for OLI and ALI images in the blue band (OLI 2 versus ALI 1) and (b) absolute difference in TOA reflectance for OLI in comparison to ALI as a function of TOA reflectance from ALI.

the earth–sun distance in astronomical units and  $\theta_s$  is the solar zenith angle.

Geometric correction frequently executes image resampling, thus reducing image quality. Therefore, to minimize the losses of spectral information from image resampling, the nearest-neighbour resampling method was used to implement geometric correction on ALI images based on the L8 OLI data coordinates (Transverse Mercator Projection, WGS\_1984\_UTM\_Zone)<sup>1</sup>.

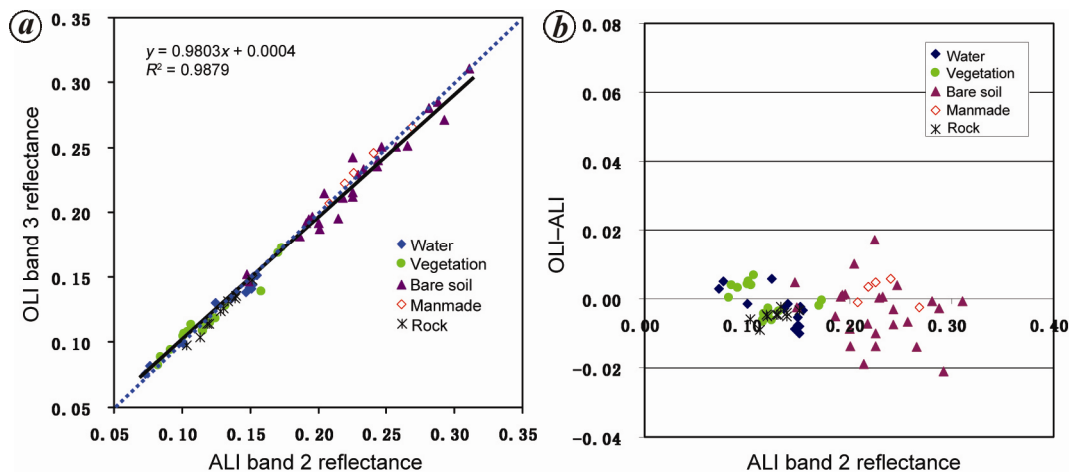
Comparisons of TOA reflectance were made at the corresponding bands between ALI and OLI over the 71 selected ROIs. Figures 2–8 show the results. The figures relate TOA reflectance of OLI to the corresponding TOA reflectance of ALI. Each data point on the plots indicates an average of all pixels in a specific ROI. The plots of OLI TOA reflectance are displayed as a function of ALI TOA reflectance. The 1 : 1 line is also plotted for reference, and a least squares fit has been made to the data for

each band<sup>1</sup>. The figures also show absolute difference in TOA reflectance between ALI and OLI.

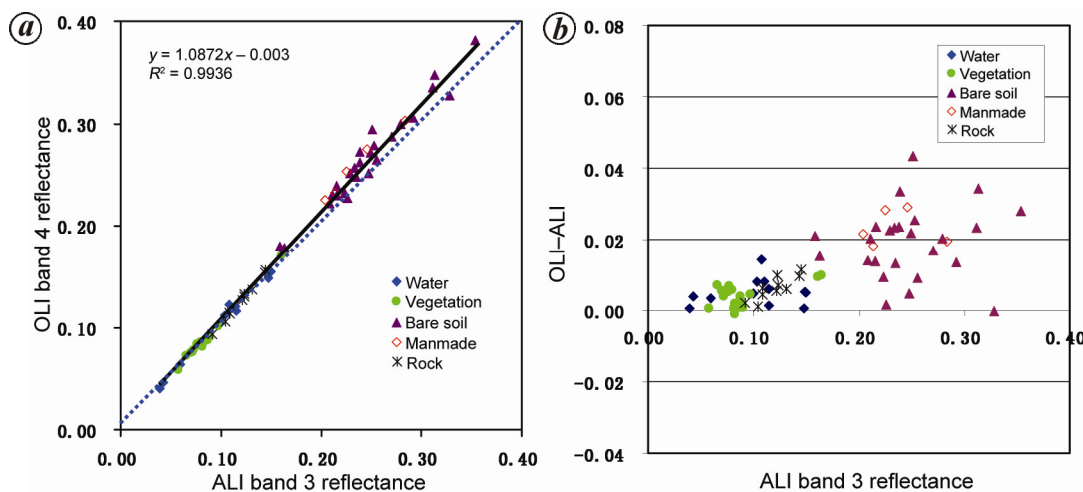
Figure 2 summarizes the TOA reflectance comparison results for OLI 1 and ALI 1P. The coefficient of determination (0.9622) and slope (0.9652) of the regression line are close to 1. The absolute difference plots indicate that difference in TOA reflectance using OLI 1 relative to ALI 1P data is from  $-0.02$  to  $0.017$ .

Figure 3 shows the TOA reflectance comparison results for OLI 2 and ALI 1. The coefficient of determination (0.9780) and slope (1.0059) of the regression line are close to 1. The absolute difference plots indicate that difference in TOA reflectance using OLI 2 relative to ALI 1 data is from  $-0.014$  to  $0.023$ .

Figure 4 summarizes the TOA reflectance comparison results for OLI 3 and ALI 2. The coefficient of determination (0.9879) and slope (0.9803) of the regression line are close to 1. The absolute difference plots indicate that



**Figure 4.** Scatter plots of (a) mean TOA reflectance of all ROIs for OLI and ALI images in the green band (OLI 3 versus ALI 2) and (b) absolute difference in TOA reflectance for OLI in comparison to ALI as a function of TOA reflectance from ALI.



**Figure 5.** Scatter plots of (a) mean TOA reflectance of all ROIs for OLI and ALI images in the red band (OLI 4 versus ALI 3) and (b) absolute difference in TOA reflectance for OLI in comparison to ALI as a function of TOA reflectance from ALI.

difference in TOA reflectance using OLI 3 relative to ALI 2 data is from  $-0.021$  to  $0.018$ .

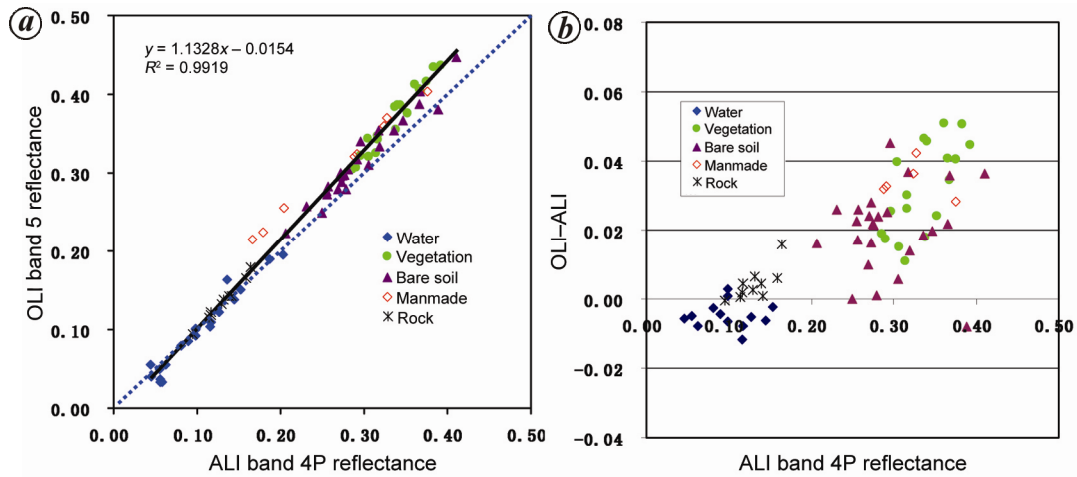
Figure 5 shows the TOA reflectance comparison results for OLI 4 and ALI 3. The coefficient of determination ( $0.9936$ ) and slope ( $1.0872$ ) of the regression line are close to 1. The absolute difference plots show that all the data points lie above the zero line, indicating ALI underestimates TOA reflectance in comparison to OLI. Each land-cover type behaves differently: water, vegetation and rock appear to estimate up to  $0.017$  lower TOA reflectance, bare soil up to  $0.044$  and man-made up to  $0.030$  lower TOA reflectance.

Figure 6 summarizes the TOA reflectance comparison results for OLI 5 and ALI 4P. The coefficient of determination ( $0.9919$ ) of the regression line is extremely close to 1. The absolute difference plots show a trend that the

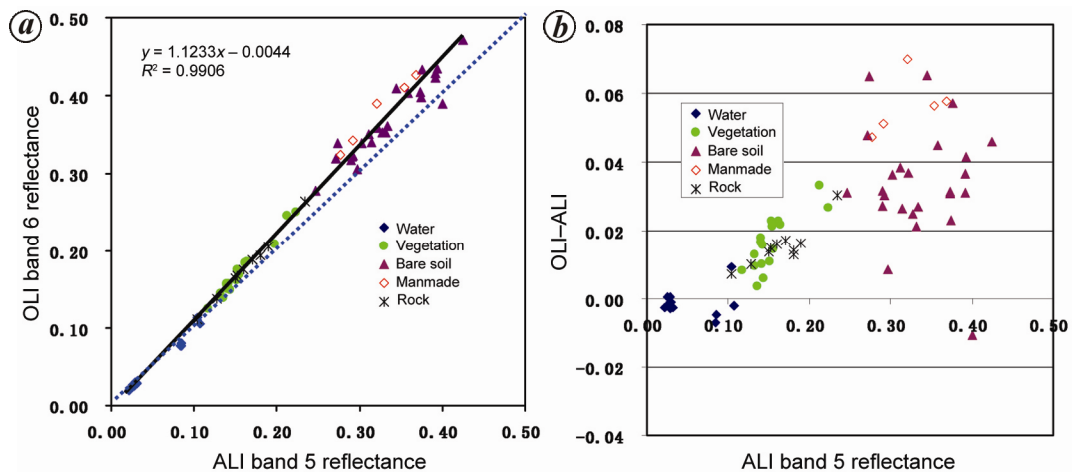
absolute difference in TOA reflectance between OLI 5 and ALI 4P is from  $-0.012$  to  $0.051$ , and increases with increase in TOA reflectance.

Figure 7 summarizes the TOA reflectance comparison results for OLI 6 and ALI 5. The coefficient of determination ( $0.9906$ ) of regression line is extremely close to 1. The absolute difference plots also show a trend that the absolute difference in TOA reflectance between OLI 6 and ALI 5 is from  $-0.01$  to  $0.07$ , and increases with increase in TOA reflectance.

Figure 8 summarizes the TOA reflectance comparison results for OLI 7 and ALI 7. The coefficient of determination ( $0.9921$ ) of the regression line is extremely close to 1. The absolute difference plots also show a trend that the absolute difference in TOA reflectance between OLI 7 and ALI 7 is from  $-0.004$  to  $0.075$ , and increases with increase in TOA reflectance.



**Figure 6.** Scatter plots of (a) mean TOA reflectance of all ROIs for OLI and ALI images in the band (OLI 5 versus ALI 4P) and (b) absolute difference in TOA reflectance for OLI in comparison to ALI as a function of TOA reflectance from ALI.

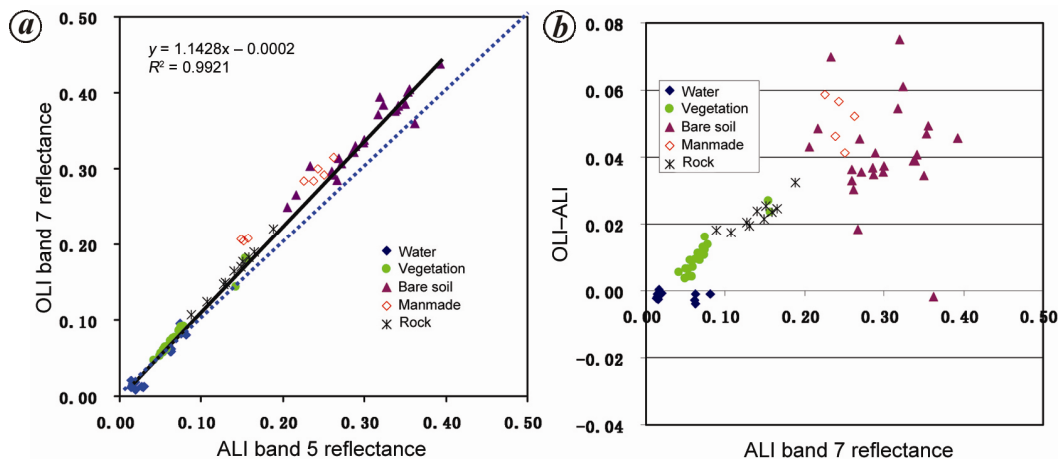


**Figure 7.** Scatter plots of (a) mean TOA reflectance of all ROIs for OLI and ALI images in the SWIR band (OLI 6 versus ALI 5) and (b) absolute difference in TOA reflectance for OLI in comparison to ALI as a function of TOA reflectance from ALI.

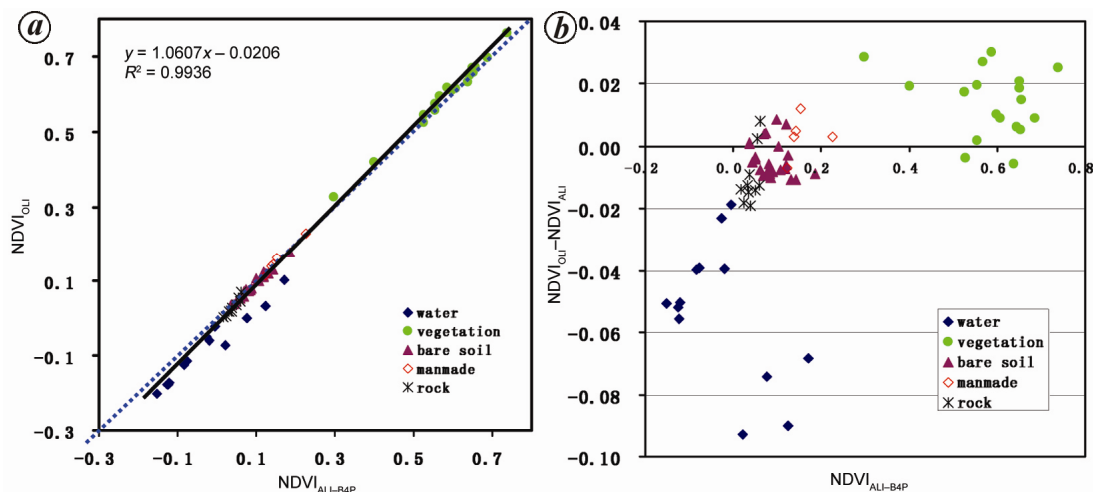
Figure 9 summarizes the NDVI derived from TOA reflectance comparison results for  $NDVI_{OLI}$  ( $NDVI$  of OLI) and  $NDVI_{ALI\_4P}$  ( $NDVI_{ALI\_4P}$  denotes ALI NDVI calculated by band 4P). The coefficient of determination (0.9936) and slope (1.0607) of the regression line are close to 1. The absolute difference plots show that all the data points of water lie below the zero line, and differences in NDVI of water using  $NDVI_{OLI}$  relative to  $NDVI_{ALI\_4P}$  data are from  $-0.10$  to  $-0.018$ . However, the absolute differences in NDVI of the other land-cover types, including vegetation, bare soil, man-made and rock, are between  $-0.02$  and  $0.03$ .

Table 5 shows the relationship between NDVI and TOA reflectance of L8 OLI and EO-1 ALI. There is a high correlation between OLI and ALI, with the coefficients of determination ranging from 0.962 to 0.994.

In conclusion, comparisons were made between EO-1 ALI and L8 OLI through orbital and imaging parameters, spectral response characteristic and spectral characteristic. Seventy-one ROIs were chosen from the six image pairs for EO-1 ALI and L8 OLI, including the land-cover categories of water, vegetation, rock, man-made and bare soil. The results indicate the following: (i) Spectral characteristics (e.g. TOA reflectance and NDVI) of L8 OLI have high correlation with those of EO-1 ALI. The coefficients of determination and slopes of those regression lines are close to 1. Accordingly, it is feasible that TOA reflectance and NDVI L8 OLI images complement and substitute those from EO-1 ALI. (ii) The absolute differences in spectral characteristics between the two sensors slightly change with the bands and land-cover types. There is a trend that the absolute differences in



**Figure 8.** Scatter plots of (a) mean TOA reflectance of all ROIs for OLI and ALI images in the SWIR band (OLI 7 versus ALI 7) and (b) absolute difference in TOA reflectance for OLI in comparison to ALI as a function of TOA reflectance from ALI.



**Figure 9.** Scatter plots of (a) mean NDVI derived from TOA reflectance of all ROIs for OLI and ALI images and (b) absolute difference in NDVI for OLI in comparison to ALI as a function of NDVI from ALI.

**Table 5.** Relation between NDVI and TOA reflectance of L8 OLI and EO-1 ALI

Spectral characteristics	Y/X	Expression	R <sup>2</sup>
TOA reflectance	OLI 1/ALI 1P	$y = 0.9652x + 0.0012$	0.962
	OLI 2/ALI 1	$y = 1.0059x - 0.0026$	0.978
	OLI 3/ALI 2	$y = 0.9803x + 0.0004$	0.988
	OLI 4/ALI 3	$y = 1.0872x - 0.003$	0.994
	OLI 5/ALI 4P	$y = 1.1328x - 0.0154$	0.992
	OLI 6/ALI 5	$y = 1.1233x - 0.0044$	0.991
	OLI 7/ALI 7	$y = 1.1428x - 0.0002$	0.992
NDVI	NDVI <sub>OLI</sub> /NDVI <sub>ALI-4P</sub>	$y = 1.0607x - 0.0206$	0.994

TOA reflectance increase with increase in wavelength, and the absolute differences in TOA reflectance of vegetation, man-made and bare soil are slightly greater than those of other land-cover types.

1. Zhang, X. and Tian, Q., Comparison of spectral characteristics between EO-1 ALI and IRS-P6 LISS-III imagery. *Curr. Sci.*, 2015, **108**, 954–960.

2. Middleton, E. M. *et al.*, The Earth Observing One (EO-1) satellite mission: over a decade in space. *IEEE J. Sel. Top. Appl. Earth Obs. Remote Sensing*, 2013, **6**, 243–256.  
 3. Lobell, D. B. and Asner, G. P., Comparison of Earth Observing-1 ALI and Landsat ETM+ for crop identification and yield prediction in Mexico. *IEEE Trans. Geosci. Remote Sensing*, 2003, **41**, 1277–1282.  
 4. Thome, K. J., Biggar, S. F. and Wisniewski, W., Cross comparison of EO-1 sensors and other earth resources sensors to Landsat-7

- ETM+ using railroad valley playa. *IEEE Trans. Geosci. Remote Sensing*, 2003, **41**, 1180–1188.
5. Chander, G., Meyer, D. J. and Helder, D. L., Cross calibration of the Landsat-7 ETM+ and EO-1 ALI sensor. *IEEE Trans. Geosci. Remote Sensing*, 2004, **42**, 2821–2831.
  6. Donegan, S. J. and Flynn, L. P., Comparison of the response of the Landsat 7 Enhanced Thematic Mapper Plus and the Earth Observing-1 Advanced Land Imager over active lava flows. *J. Volcanol. Geotherm. Res.*, 2004, **135**, 105–126.
  7. Chander, G., Angal, A., Choi, T. and Xiong, X., Radiometric cross-calibration of EO-1 ALI with L7 ETM+ and Terra MODIS sensors using near-simultaneous desert observations. *IEEE J. Sel. Top. Appl. Earth Obs. Remote Sensing*, 2013, **6**, 386–399.
  8. Petropoulos, G. P., Kontoes, C. C. and Keramitsoglou, I., Land cover mapping with emphasis to burnt area delineation using co-orbital ALI and Landsat TM imagery. *Int. J. Appl. Earth Obs. Geoinf.*, 2012, **18**, 344–355.
  9. Pu, R., Bell, S., Meyer, C., Baggett, L. and Zhao, Y., Mapping and assessing seagrass along the western coast of Florida using Landsat TM and EO-1 ALI/Hyperion imagery. *Estuarine Coastal Shelf Sci.*, 2012, **115**, 234–245.
  10. Price, J. C., Calibration of satellite radiometers and the comparison of vegetation indices. *Remote Sensing Environ.*, 1987, **21**, 15–27.
  11. Belchansky, G. I. and Douglas, D. C., Integrating remotely sensed data with an ecosystem model to estimate net primary productivity in East Asia. *Remote Sensing Environ.*, 2002, **81**, 58–66.
  12. Francis, S. C., Richard, F. and Jing, C., Comparison and evaluation of medium resolution imaging spectrometer leaf area index products across a range of land use. *Remote Sensing Environ.*, 2010, **114**, 950–960.
  13. Yu, T. *et al.*, Comparison of the influence factors on NDVI for CCD camera and WFI imager on CBERS-02. *Science China Ser. E (Supp. I)*, 2005, **48**, 100–115.
  14. Li, G. *et al.*, Comparison of spectral characteristics between China HJ1-CCD and Landsat 5 TM imagery. *IEEE J. Sel. Top. Appl. Earth Obs. Remote Sensing*, 2013, **6**, 139–148.
  15. Fensholt, R., Sandholt, I. and Stisen, S., Evaluating MODIS, MERIS, and VEGETATION vegetation indices using *in situ* measurements in a semiarid environment. *IEEE Trans. Geosci. Remote Sensing*, 2006, **44**, 1774–1786.
  16. Chander, G., Markham, B. L. and Helder, D. L., Summary of current radiometric calibration coefficients for Landsat MSS, TM, ETM+, and EO-1 ALI sensors. *Remote Sensing Environ.*, 2009, **113**, 893–903.

ACKNOWLEDGEMENTS. This study was supported by the Open Fund of Key Laboratory of Meteorology and Ecological Environment of Hebei Province (grant no. Z201607Y) and the National Natural Science Foundation of China (grant no. 41201461).

Received 7 August 2016; revised accepted 30 November 2016

doi: 10.18520/cs/v112/i11/2288-2295

## Geomorphic evidence of late Quaternary displacement of the Karakoram Fault in Nubra and Shyok valleys, Ladakh Himalaya

Watinaro Imsong<sup>1,3,\*</sup>, Falguni Bhattacharya<sup>2</sup>,  
Rajeeb Lochan Mishra<sup>1</sup> and Sarat Phukan<sup>3</sup>

<sup>1</sup>Wadia Institute of Himalayan Geology, Dehradun 248 001, India

<sup>2</sup>Institute of Seismological Research, Gandhi Nagar 382 421, India

<sup>3</sup>Department of Geological Sciences, Gauhati University, Guwahati 781 013, India

**The present study ascertains the spatial variability in the extent of activity of the Karakoram Fault (KF) in Nubra and Shyok river valleys (Karakoram), which was known to be active during the Holocene. Towards this we have used conventional morphometric indices supported by geomorphological observations on the pattern of alluvial and bedrock streams, alluvial fan geometry and moraines. The right lateral displacement associated with KF is geomorphologically expressed by the lateral deflections of the bedrock and alluvial streams toward northwest–southeast as they cut across the Fault. Indirect age estimates inferred based on slip rate of KF suggest that the deflection of bedrock streams with prominent shutter ridges is the cumulative expression of activity of KF since the middle Pleistocene, which continued till the late Holocene.**

**Keywords:** Alluvial and bedrock streams, geomorphic evidence, morphometry, right lateral displacement.

THE convergent tectonics of the Himalaya has not changed considerably since the Miocene, and the orogeny manifests a quasi-steady state<sup>1</sup>. The trace of deformational episodes that progressed in space and time can be seen in the sequential evolution of major terrain boundary thrusts<sup>1</sup>. In the northwestern Himalaya, the Indus Suture Zone (ISZ) and Shyok Suture Zone (SSZ) are displaced by the right-lateral Karakoram Fault (KF) system<sup>1–3</sup>. The Shyok and Nubra valleys are intersected by KF, and the southern end of the Fault merges with the Indus (Yarlung) Suture Zone near Mount Kailas<sup>2,4</sup>. Separating the central Karakoram and Ladakh range<sup>5,6</sup>, the KF is a NW–SE striking, normal–dextral fault which has displaced the Jurassic–Cretaceous Karakoram batholith from the Gangdese batholith with a displacement of ~1000 km causing the eastward extrusion of the Tibetan Plateau<sup>2,7,8</sup>. According to Searle *et al.*<sup>9–11</sup>, although KF is active today, the right lateral offset is probably less than ~120–150 km and the displacement continued since early to mid-Miocene. Studies suggest that KF is undergoing transpressional and transtensional tectonics<sup>8,12–14</sup>. According to Searle *et al.*<sup>6</sup>, ~150 km right-lateral displacement with a vertical

\*For correspondence. (e-mail: imsongnar@gmail.com)